

In-situ fabricated anisotropic halide perovskite nanocrystals in polyvinylalcohol nanofibers: Shape tuning and polarized emission

Linghai Meng¹, Changgang Yang³, Jingjia Meng¹, Yongzhi Wang², Yong Ge¹, Ziqiang Shao² (✉), Guofeng Zhang³, Andrey L. Rogach⁴, and Haizheng Zhong¹ (✉)

¹ Beijing Key Laboratory of Nanophotonics and Ultrafine Optoelectronic Systems, School of Materials Science and Engineering, Beijing Institute of Technology, Beijing 100081, China

² Beijing Engineering Research Center of Cellulose and Its Derivatives, School of Materials Science and Engineering, Beijing Institute of Technology, Beijing 100081, China

³ State Key Laboratory of Quantum Optics and Quantum Optics Devices, Institute of Laser Spectroscopy, Shanxi University, Taiyuan 030006, China

⁴ Department of Materials Science and Engineering, and Centre for Functional Photonics (CFP), City University of Hong Kong, Hong Kong 999077, China

© Tsinghua University Press and Springer-Verlag GmbH Germany, part of Springer Nature 2019

Received: 13 January 2019 / Revised: 18 February 2019 / Accepted: 19 February 2019

ABSTRACT

We report an *in-situ* fabrication of halide perovskite ($\text{CH}_3\text{NH}_3\text{PbX}_3$, CH_3NH_3 = methylammonium, MA, X = Cl, Br, I) nanocrystals in polyvinylalcohol (PVA) nanofibers (MAPbX₃@PVA nanofibers) through electrospinning a perovskite precursor solution. With the content of the precursors increased, the resulting MAPbBr₃ nanocrystals in PVA matrix changed the shape from ellipsoidal to pearl-like, and finely into rods-like. Optimized MAPbBr₃@PVA nanofibers show strong polarized emission with the photoluminescence quantum yield of up to 72%. We reveal correlations between the shape of *in-situ* fabricated perovskite nanocrystals and the polarization degree of their emission by comparing experimental data from the single nanofiber measurements with theoretical calculations. Polarized emission of MAPbBr₃@PVA nanofibers can be attributed to the dielectric confinement and quantum confinement effects. Moreover, nanofibers can be efficiently aligned by using parallel positioned conductor strips with an air gap as collector. A polarization ratio of 0.42 was achieved for the films of well-aligned MAPbBr₃@PVA nanofibers with a macroscale size of 0.5 cm × 2 cm, which allows potential applications in displays, lasers, waveguides, etc.

KEYWORDS

lead halide perovskite, nanofibers, electrospinning, anisotropy, polarized emission

1 Introduction

In the recent few years, perovskite nanocrystals (PNCs) have been intensively investigated as functional materials for optoelectronic applications, including light-emitting devices [1–4], lasers [5–7], down-shifting applications [8–13] due to their superior photoluminescence (PL) with high quantum yield (QY), narrow full width at half maximum (FWHM), tunable band gap as well as easy processibility [14]. In addition to these features, anisotropic PNCs show polarized emission [15]. By adapting the strategies from the synthesis of conventional II-VI semiconductor NCs, anisotropic PNCs, such as nanoplatelets, nanowires, and nanorods have been successfully fabricated, and explored for display technology [16–18], optical waveguides [19], lasers [20, 21] and polarization-sensitive photodetectors [22–24]. Fabrication of well-aligned anisotropic perovskite nanostructures is essential to make use of their properties. Several methods have been developed to align anisotropic PNCs into ordered patterns, including template-assisted assembly [25–28], mechanical stretching [17, 18, 29], and electrospinning [30].

Electrospinning is a versatile technique for fabrication of composite nanofibers, with advantages of both the morphology tuning and a continuous production [31]. In the previous works, preformed PNCs have been embedded into polymer nanofibers and explored for light-emitting applications [32–36]. This technique can be

optimized further toward highly luminescent, color-tunable PNC based materials with polarized emissions. Previously, we have reported on the *in-situ* fabrication of PNCs in polymer matrix, and demonstrated their advantages for the device integration [10, 14]. In this work, we report the shape tuning of the *in-situ* fabricated MAPbX₃ NCs embedded into the polyvinylalcohol (PVA) nanofibers by using the electrospinning method. We demonstrate the alignment of composite nanofibers by using parallel positioned conductor strips with an air gap as collector. Using single nanofiber PL measurements, we have revealed correlations between the shape of the *in-situ* fabricated PNCs and the polarization degree of their emission. The polarization anisotropy has been explained by applying the dielectric ellipsoid model and taking into consideration quantum confinement effects.

2 Experimental section

2.1 Materials

PVA ($M_w \approx 140,000$, Sigma-Aldrich) was received from Sigma-Aldrich. Lead halide salts with $\geq 98\%$ purity were purchased from Alfa Aesar. Dimethyl sulfoxide (DMSO, anhydrous, $\geq 99\%$), and methylammonium halides were purchased from Sigma-Aldrich. All chemicals were used as received without further purification.

2.2 Fabrication

Two parallel steel strips were placed 5 mm apart from each other on a glass collector to obtain aligned nanofibers. The precursor solution was partly transferred into a 10 mL syringe with a spinneret of 0.51 mm in diameter. During the spinning process, the flow rate was $0.3 \text{ mL}\cdot\text{h}^{-1}$ for the PVA polymer concentration of $125 \text{ mg}\cdot\text{mL}^{-1}$. Two electrode holders were connected to the syringe needle and the collector, respectively. The voltage was set at 20 kV, and the working distance (the distance between the tip of the needle and collector) was 15 cm. Electrospinning was conducted at 50°C and 30% relative humidity.

2.3 Materials characterizations

Scanning electron microscopy (SEM) characterizations were analyzed using Hitachi S4800 SEM machine operating at accelerating voltage of 5.0 kV. Transmission electron microscopy (TEM) characterizations were analyzed using a JEOL-JEM 2100F TEM machine operating at an acceleration voltage of 200 kV. X-ray diffraction (XRD) measurements were determined on a Bruker D8 FOCUS X-ray diffractometer, using a Cu KR radiation source (wavelength at 1.5405 \AA). The absolute PLQYs of nanofiber films were determined using a fluorescence spectrometer with an integrated sphere (C9920-02, Hamamatsu Photonics, Japan) excited at a wavelength of 405 nm using a light-emitting diode light source.

2.4 Polarization measurements

A picosecond pulsed diode laser (LDH-IB-405-B, PicoQuant) was used to excite single nanofiber. The output of the pulse laser was passed through $\lambda/2$ and $\lambda/4$ wave plate to change the polarized laser into circular polarization light. The beam was sent into a conventional inverted fluorescence microscope (IX71, Olympus) from its back side, reflected by a dichroic mirror (Di03-R405, Semrock), and focused by an oil immersion objective lens ($100\times$, 1.3 NA, Olympus) onto the upper sample surface of the glass cover slip. After filtering out the laser from the substrate, the PL photons of single nanofiber is collected the same objective lens. The PL photons are sent to a rotating achromatic half-wave plate combined with a broadband polarizing beamsplitter cube to measure the polarization ratios. The polarization beam splitter divides the PL photons into its two components which are subsequently focused through two lenses and collected by two single photon detectors (SPCM-AQR-15, PerkinElmer).

3 Results and discussion

3.1 Characterization of composite MAPbX_3 @PVA nanofibers

PVA was selected as polymeric matrix due to its well-known application as polymer materials in polarizer plates [37]. As schematically shown in Fig. 1(a), a precursor solution of methylammonium halides (MAX , $X = \text{Cl, Br, I}$), PbBr_2 and PVA at various weight ratios in DMSO solution was used for electrospinning (see Table S1 in Electronic Supplementary Material (ESM)). A liquid jet was directed toward the collector, and the solvent evaporated simultaneously during the electrospinning. When the concentration of the precursor solution approached the critical saturation, crystallization of MAPbX_3 PNCs took place within the polymer matrix. Figure 1(b) shows a SEM image of uniform and smooth MAPbBr_3 @PVA nanofibers, with an enlarged image in the insert. Figures 2(a1)–2(a5) show the TEM images of MAPbBr_3 @PVA nanofibers prepared with different mass fraction of precursor concentrations (Sample 1: 10 wt.%, Sample 2: 20 wt.%, Sample 3: 30 wt.%, Sample 4: 40 wt.%, and Sample 5: 50 wt.%). The nanofibers have an average diameter of 40–60 nm and length of several hundred micrometers. Respective high-resolution TEM images shown in Figs. 2(b1)–2(b5) confirm

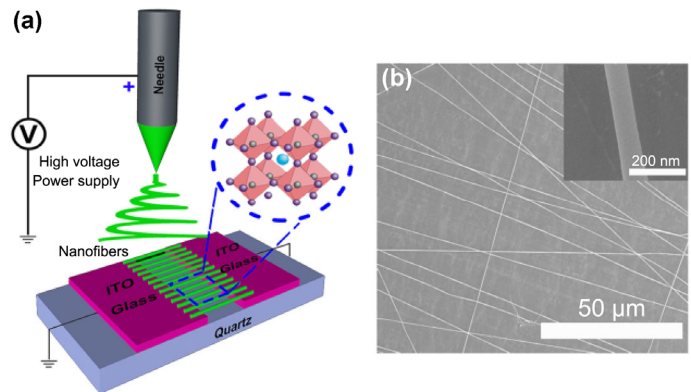


Figure 1 (a) Schematic illustration of the electrospinning set-up. The collector is composed from two conductive substrates separated by a void gap. (b) SEM image of MAPbBr_3 @PVA nanofibers; inset shows an enlarged view of a single nanofiber.

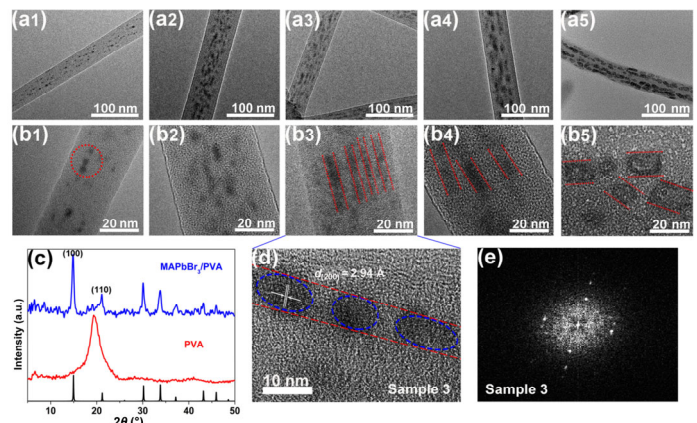


Figure 2 (a1)–(a5) TEM and (b1)–(b5) corresponding HRTEM images of MAPbBr_3 @PVA nanofibers fabricated using different precursor concentrations (see text for details). (c) XRD pattern of PVA and composite MAPbBr_3 @PVA films. (d) HRTEM image of aligned anisotropic MAPbBr_3 PNCs, and (e) the corresponding Fourier transform image.

that the *in-situ* fabricated PNCs are well-dispersed inside the polymer nanofibers, and have a different shape, from quasi-spherical to elongated, depending on the precursor concentration. As shown in Fig. 2(b1), the shape of the PNCs in the Sample 1 (precursor concentration 10 wt.%) is ellipsoidal, with diameter of $\sim 3 \text{ nm}$ and length of $\sim 4.5 \text{ nm}$. As shown in Figs. 2(b2)–2(b4), the PNC shape changes from ellipsoid (Sample 2) into pearl-like (Sample 3), and further into rod-like (Sample 4), when the precursor concentration increases from 20 wt.% to 40 wt.%. When the precursor concentration increases to 50 wt.%, the resulting PNCs (Sample 5) become larger, with the diameter of $\sim 10 \text{ nm}$ and length of $\sim 20 \text{ nm}$ (Fig. 2(b5)). More details about the size distribution of MAPbBr_3 NCs are provided in Fig. S1 in the ESM. Table 1 summarizes aspect ratios (ARs) of PNCs obtained with the different precursor concentration. We notice from HRTEM images that the long axes of the PNCs tend to align

Table 1 Aspect ratios (AR) of the PNCs obtained with different mass fraction of precursor concentration, and their emission polarization ratios (for single nanofibers and nanofiber films)

Sample	AR	Polarization ratio of single fiber	Polarization ratio of fiber film
Sample 1	1.5	0.36 ± 0.03	0.29 ± 0.02
Sample 2	2	0.39 ± 0.06	0.30 ± 0.03
Sample 3	6	0.53 ± 0.06	0.42 ± 0.03
Sample 4	4	0.45 ± 0.05	0.33 ± 0.02
Sample 5	2	0.41 ± 0.07	0.30 ± 0.04

along the PVA nanofibers, which can be attributed to stretching force during the electrospinning process. As shown in Fig. S2 in the ESM, samples with varying halide composition, namely MAPbBr_xCl_{3-x} and MAPbBr_xI_{3-x}@PVA nanofibers also contain anisotropic rods.

Figure 2(c) presents a typical XRD pattern of MAPbBr₃@PVA nanofibers. The broad diffraction peaks are ascribed to the amorphous PVA, while peaks at 14.9°, 21.3°, 30.2°, 33.7°, 43.2°, and 45.9° correspond to the lattice planes of (100), (110), (200), (210), (220), and (300) of MAPbBr₃ respectively. Compared with (100) planes, the relatively weak (110) plane diffraction peak of MAPbBr₃ NCs is observed, implying the existence of a preferred arrangement orientation in the molecular stacking [38]. This observation is supported by HRTEM observations: as shown in Figs. 2(d) and 2(e), the HRTEM image and corresponding Fourier transform (FFT) pattern confirm that the resulting PNCs are composed from oriented nanoparticles connected along {100} direction. Figure S3 in the ESM shows the XRD patterns of MAPbBr_xCl_{3-x} and MAPbBr_xI_{3-x}@PVA nanofibers. The diffraction peaks from MAPbBr_xCl_{3-x} and MAPbBr_xI_{3-x} can be well identified.

3.2 Optical properties of single MAPbX₃@PVA nanofibers

As shown in Fig. 3(a), PL peaks of MAPbBr₃@PVA nanofibers are gradually red shifted from 515 to 528 nm with increasing precursor concentration. According to Fig. 3(b), the samples show PLQYs of 49% to 72%. By varying the composition of anions (X = Cl, Br and I), PL emission can be tuned from 488 to 626 nm in the visible region (Fig. 3(a)). The emission profiles of MAPbX₃@PVA nanofibers are reasonably narrow, with FWHM from 21 to 39 nm. As shown in Fig. 3(c) and Fig. S4 in the ESM, the PL decays of MAPbX₃@PVA nanofibers are multi-exponential. In comparison with the reported MAPbBr₃ NCs in colloidal solution [8], the *in-situ* fabricated MAPbBr₃ NCs in PVA nanofibers show longer average PL lifetime (τ_{avg}) ranging from 33 to 85 ns, as shown in Fig. 3(d). The sample with the highest PLQY has the longest average PL lifetime. The long PL lifetime can be explained by reduced quantum confinement effects due to the difference of dielectric constants between PVA and air [39]. For the *in-situ* fabricated PNCs the PL emission mainly originates from the recombination of free electrons and holes in MAPbBr₃ NCs. The long PL lifetime and high PLQY indicate that the resulting *in-situ* fabricated MAPbBr₃ NCs encapsulated by PVA fibers have little amount of surface defects.

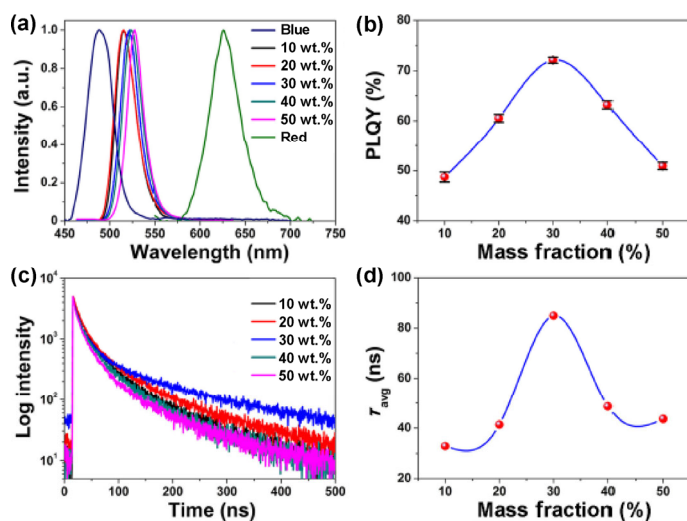


Figure 3 (a) PL spectra of the composite MAPbBr₃@PVA nanofiber films, and (b) the plot of their PLQY as a function of the mass fraction of precursor concentration. (c) Time-resolved PL spectra of MAPbBr₃@PVA nanofiber films, and (d) the plot of their average PL lifetimes as a function of the mass fraction of precursor concentrations. Blue connecting lines in (b) and (d) are just guides for eye.

Polarization is an inherent feature of anisotropic nanostructures [40, 41]. The polarization ratio can be presented as the ratio $P = (I_{\parallel} - I_{\perp}) / (I_{\parallel} + I_{\perp})$, where I_{\parallel} and I_{\perp} are light intensities in the directions parallel and perpendicular to the direction of the composite nanofibers. According to the previous studies of anisotropic CdSe nanostructures, the polarization anisotropy of 1D semiconductor nanomaterials usually combines both electronic contribution and dielectric effects [42, 43]. To investigate the polarization properties of MAPbBr₃@PVA nanofibers, we performed polarization measurements of the PL emission (P_{em}) and the PL excitation (P_{ex}) on single nanofibers, with a set-up for the PL measurements shown in Fig. S5 in the ESM [44]. Figure 4(a) presents a confocal scanning PL image of a single nanofiber, with several bright spots all over its length. To clarify the correlation between the shape of PNCs embedded into PVA nanofibers and the polarization ratio of their emission, we measured the emission polarization property of nanofibers by single particle polarization microscopy. Figures 4(b)–4(f) provide polarization histograms for representative single MAPbBr₃@PVA nanofibers obtained while using different precursor concentrations. The histograms are obtained after measurements of 20 bright spots for each nanofiber, and the results are summarized in Table 1. It can be concluded that the polarization ratio of the *in-situ* fabricated PNCs in PVA nanofibers is correlated with their ARs. With the increase of AR, the polarization ratio increased from 0.36 ± 0.03 for the Sample 1 with AR of 1.5 to 0.53 ± 0.06 for the Sample 3 with AR of 6. A similar phenomenon has been previously observed for CdSe nanorods [45, 46].

Selective polarization excitation measurements can clarify the effects of anisotropic electronic states [47]. We measured the polarization anisotropy of MAPbBr₃@PVA nanofibers at different excitation wavelengths (Fig. 5(a)), namely at 405 and 473 nm. Figure 5(b) shows the integrated PL intensity as a function of polarization angle (φ), where φ is defined as the angle between the long axis of MAPbBr₃@PVA nanofibers and the polarized excitation light. The variation of the PL intensity with the polarization angle follows a sinusoidal function, and the PL intensity of E_{\parallel} ($\varphi = 0^\circ$) is two times higher than E_{\perp} ($\varphi = 90^\circ$). The polarization ratio measured at 405 and 473 nm are 0.33 ± 0.02 , and 0.42 ± 0.03 , respectively. The larger polarization at the longer wavelength excitation suggests that the electronic transition in MAPbBr₃ NCs also contribute to excitation anisotropy [48, 49]. It is also noted that the polarization excitation anisotropy is less than the polarization emission anisotropy for the same sample. When the excitation photon has an energy well above the band-gap, the number of possible electronic transitions increases rapidly, and the electronic contribution to the polarization of the excitation decreases. However, the emission still occurs from the same band-edge states, and the emission profile and its polarization remain fixed regardless of the energy of excitation.

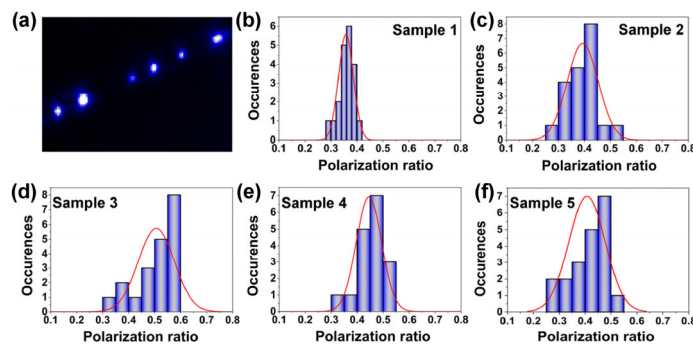


Figure 4 (a) A confocal scanning PL image of a single MAPbBr₃@PVA nanofiber. (b)–(f) Polarization ratio histograms for MAPbBr₃@PVA nanofibers obtained with different mass fraction of the precursor concentrations (Sample 1: 10 wt.%; Sample 2: 20 wt.%, Sample 3: 30 wt.%, Sample 4: 40 wt.% and Sample 5: 50 wt.%, respectively)

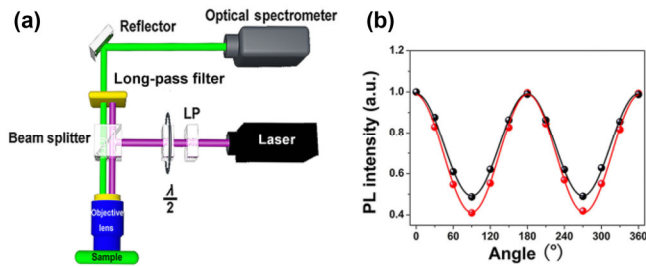


Figure 5 (a) Experimental setup for single nanofiber polarization excitation microscopy. (b) Polarization anisotropy of the emission of the Sample 3 (30 wt.%) excited at 405 nm (black) and at 473 nm (red).

Thus, the excitation well above the band-gap must be rather insensitive to the polarization of the exciting light, leading to a low $P_{\text{ex}} (< P_{\text{em}})$ [50, 51].

Considering anisotropic PNCs embedded in a dielectric matrix, their polarization anisotropy can be described by adapting physical models of the dielectric confinement effects and quantum confinement effects, as illustrated in Fig. 6(a). The incident circular polarized light is modulated into elliptic polarized light due to the change of dielectric constant (ϵ) at the interface of PVA nanofiber and air; this light interacts with embedded anisotropic PNCs to generate excitons, which subsequently recombine to give polarized PL emission. The polarization modulation of PVA fiber can be described by Eqs. (1) and (2) [52]

$$E_{1//} = E_{0//} \quad (1)$$

$$E_{1\perp} = \frac{2\epsilon_0}{\epsilon_0 + \epsilon_1} E_{0\perp} \quad (2)$$

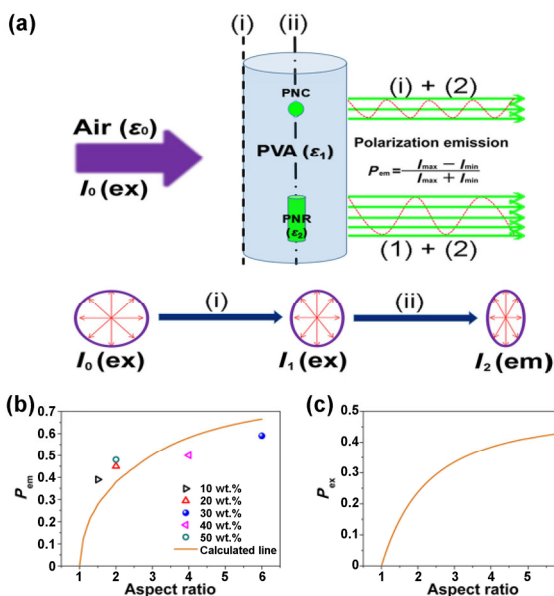


Figure 6 (a) Schematic diagram illustrating the mechanism for polarized emission of anisotropic perovskite rods. Polarization emission is mainly due to dielectric confinement effect (1) and quantum confinement effect (2). PVA nanofibers can be considered as a cylindrical model, and ellipsoidal model can be used for nanorods. Process (i): Circularly polarized light with an intensity $I_0(\text{ex})$ enters the interface between the air (ϵ_0) and the polymer (ϵ_1), which is transformed into elliptically polarized light ($I_1(\text{ex})$) due to the variation of dielectric constants. (ii): $I_1(\text{ex})$ propagates to the interface between the PVA and perovskite rods; the electric field distribution inside nanorods is treated by ellipsoidal model. The $I_1(\text{ex})$ excites the nanorods to produce higher polarized emission ($I_2(\text{em})$). The polarization emission of small AR PNCs is due to the quantum confinement effect. (b) and (c) Dependence of the P_{em} and P_{ex} on aspect ratios of the perovskite rods. Solid orange lines correspond to the calculated polarization of MAPbBr₃@PVA nanofibers using Eqs. (7) and (8). The points are experimentally determined values.

where E_0 is an external electric field, with its parallel component, $E_{0//}$ and perpendicular component, $E_{0\perp}$. ϵ_0 is the dielectric constant of air, and ϵ_1 is the dielectric constant of PVA.

The interaction between the incident light and the PNCs within PVA fibers can be described by applying dielectric ellipsoid model. According to this model, the dielectric contrast between PNCs and PVA gives rise to a depolarization field, which attenuates the applied electric field perpendicular to the long axis of PNC. The anisotropy of the electric field induces the polarization emission and excitation for PNCs [43, 45, 53]. It can be described by the ratio (k) of field strength between the major and minor axes of PNCs [54]

$$k = \frac{\epsilon_1 + (\epsilon_2 - \epsilon_1)n_{//}}{\epsilon_1 + (\epsilon_2 - \epsilon_1)n_{\perp}} \quad (3)$$

where ϵ_2 is the dielectric constant of the PNC and the depolarization factors, $n_{//,\perp}$ depend on axes (a, c) of the ellipsoid as [53]

$$n_{//} = \frac{1 - e^2}{2e^3} \left(\ln \frac{1 + e}{1 - e} - 2e \right) \quad (4)$$

$$n_{\perp} = \frac{1}{2}(1 - n_{//}) \quad (5)$$

$$e = \sqrt{1 - a^2 / c^2} \quad (6)$$

where e is the eccentricity of the ellipsoid.

The polarized emission (P_{em}) and excitation (P_{ex}) can be calculated by combining equations 3 to 6 as following [54, 55]

$$P_{\text{em}} = \frac{9(k^2 - 1)^2}{23k^4 + 34k^2 + 3} \quad (7)$$

$$P_{\text{ex}} = \frac{1 - k^2}{1 + k^2} \quad (8)$$

We then calculated the theoretical polarization anisotropy by adapting the dielectric constants of bulk materials ($\epsilon_{\text{PVA}} = 2.1$, $\epsilon_{\text{MAPbBr}_3} = 5.1$). Figures 6(b) and 6(c) show how polarization emission and excitation depend on the ARs of elongated PNCs. Compared with experimental results obtained from single nanofiber PL measurements, the calculated values are comparable with the maximum value determined in the experiment. We note that the polarization anisotropy of emission obtained from single nanofiber based experimental measurements are slightly larger than the calculated values for PNCs with AR of 1–3. Because the diameter of PNCs in PVA nanofibers is approximately two times the value of the Bohr radius of MAPbBr₃ (~ 2 nm) [56], this observation can be explained by the enhanced polarization due to the quantum confinement effects.

3.3 Aligned MAPbX₃@PVA nanofibers in a film

Although single MAPbX₃@PVA nanofiber show polarized emission, they have to be aligned in a film to make use of the polarized PL of the ensemble. By adapting parallel positioned conductor strips with an air gap, we fabricated macroscopically aligned nanofiber samples with a size of 0.5 cm × 2 cm. The emission anisotropy of the MAPbBr₃@PVA nanofiber film is shown in Fig. 7. The polar diagram of the PL intensity dependence on the polarization angle is given in Fig. 7(a), with the maximum along the long axis and the highest P_{em} around 0.42 ± 0.03 . The polarization ratios of the aligned MAPbBr₃@PVA nanofiber films are summarized in Table 1. Figures 7(b) and 7(c) show polarization microscopy images of the films, which demonstrate that the polarization is well maintained when aligning the nanofibers over a large area. As clear evidence of the parallel alignment of the MAPbBr₃@PVA nanofibers, a bright image is obtained when the polarizer is parallel to the nanofibers ($\theta = 0^\circ$) and a dark image is obtained when the polarizer is perpendicular to nanofibers ($\theta = 90^\circ$). Figures 7(d)–7(f) show the

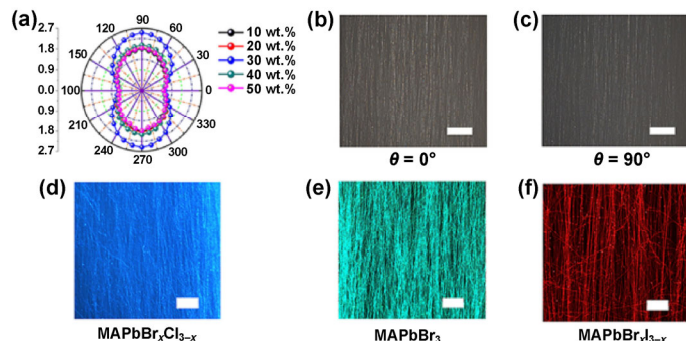


Figure 7 (a) The polarized emission of the aligned MAPbBr₃@PVA nanofiber films with different mass fraction of precursor concentrations, as indicated. (b) and (c) Polarization microscopy images of the aligned MAPbBr₃@PVA nanofiber film (Sample 3), scale bar: 100 μm. (d)–(f) Fluorescent optical microscope images of MAPbX₃@PVA nanofiber films, scale bar: 100 μm.

fluorescent optical microscopy images of MAPbX₃@PVA nanofiber films, validating the versatility of electrospinning method in fabricating highly luminescent perovskite nanofibers with macroscale alignment. To illustrate the potential scale-up fabrication, we fabricated a large area film of 56 cm² by collecting MAPbBr₃@PVA nanofibers on a high-speed rotating drum (3,500 rpm/min) with a precursor concentration 30 wt.% (see Fig. S6 in the ESM). These MAPbBr₃@PVA nanofibers have potential to apply as optical films for enhancing the display backlights [57, 58].

4 Conclusions

We demonstrated the *in-situ* fabrication of MAPbX₃ PNCs embedded in PVA nanofiber by electrospinning a perovskite precursors solution mixed with PVA. As a result, we have obtained highly luminescent MAPbX₃@PVA nanofibers with polarized emission. By increasing the concentration of the precursor solution, the resulting *in-situ* fabricated MAPbX₃ PNCs changed from ellipsoidal shape into anisotropic rods. By changing composition of halides, the emission spectra of MAPbX₃ PNCs can be tuned from 400 to 700 nm. From single nanofiber PL measurements, we demonstrated correlations between polarization anisotropy and shape evolution of the MAPbBr₃ NCs in PVA nanofiber. The emission polarization ratio increased from 0.36 ± 0.03 to 0.53 ± 0.06 when their AR increased from 1.5 to 6. Through comparison between the experimental data and theoretical calculations, the polarization of the MAPbBr₃@PVA nanofibers was attributed to the dielectric confinement effects with quantum confinement effects. Finally, we illustrated that the electrospinning method has a potential to fabricate large-area aligned nanofiber films, by adapting parallel positioned conductor strips with an air gap as a collection electrode. An emission polarization ratio of 0.42 ± 0.03 was achieved for the MAPbX₃@PVA film of 0.5 cm × 2 cm in size. The MAPbX₃@PVA nanofibers with polarized emission demonstrated here are interesting materials for several applications, such as displays, lasers, waveguides, and so on.

Acknowledgements

Financial support from the National Natural Science Foundation of China (NSFC)/Research Grants Council (RGC) Joint Research project 51761165021 and N_CityU108/17 is gratefully acknowledged.

Electronic Supplementary Material: Supplementary material (experimental section, detail of polarization measurements, SEM, XRD, TRPL and polarization emission measurements) is available in the online version of this article at <https://doi.org/10.1007/s12274-019-2353-4>.

References

- [1] Kim, Y. H.; Cho, H.; Lee, T. W. Metal halide perovskite light emitters. *Proc. Natl. Acad. Sci. USA* **2016**, *113*, 11694–11702.
- [2] Lozano, G. The role of metal halide perovskites in next-generation lighting devices. *J. Phys. Chem. Lett.* **2018**, *9*, 3987–3997.
- [3] Han, D. B.; Imran, M.; Zhang, M. J.; Chang, S.; Wu, X. G.; Zhang, X.; Tang, J. L.; Wang, M. S.; Ali, S.; Li, X. G. et al. Efficient light-emitting diodes based on *in situ* fabricated FAPbBr₃ nanocrystals: The enhancing role of the ligand-assisted reprecipitation process. *ACS Nano* **2018**, *12*, 8808–8816.
- [4] Song, J. Z.; Li, J. H.; Li, X. M.; Xu, L. M.; Dong, Y. H.; Zeng, H. B. Quantum dot light-emitting diodes based on inorganic perovskite cesium lead halides (CsPbX₃). *Adv. Mater.* **2015**, *27*, 7162–7167.
- [5] Veldhuis, S. A.; Boix, P. P.; Yantara, N.; Li, M. J.; Sum, T. C.; Mathews, N.; Mhaisalkar, S. G. Perovskite materials for light-emitting diodes and lasers. *Adv. Mater.* **2016**, *28*, 6804–6834.
- [6] Wang, Y.; Sun, H. D. All-inorganic metal halide perovskite nanostructures: From photophysics to light-emitting applications. *Small Methods* **2018**, *2*, 1700252.
- [7] Yakunin, S.; Protesescu, L.; Krieg, F.; Bodnarchuk, M. I.; Nedelcu, G.; Humer, M.; De Luca, G.; Fiebig, M.; Heiss, W.; Kovalenko, M. V. Low-threshold amplified spontaneous emission and lasing from colloidal nanocrystals of caesium lead halide perovskites. *Nat. Commun.* **2015**, *6*, 8056.
- [8] Protesescu, L.; Yakunin, S.; Bodnarchuk, M. I.; Krieg, F.; Caputo, R.; Hendon, C. H.; Yang, R. X.; Walsh, A.; Kovalenko, M. V. Nanocrystals of cesium lead halide perovskites (CsPbX₃, X = Cl, Br, and I): Novel optoelectronic materials showing bright emission with wide color gamut. *Nano Lett.* **2015**, *15*, 3692–3696.
- [9] Zhang, F.; Zhong, H. Z.; Chen, C.; Wu, X. G.; Hu, X. M.; Huang, H. L.; Han, J. B.; Zou, B. S.; Dong, Y. P. Brightly luminescent and color-tunable colloidal CH₃NH₃PbX₃ (X = Br, I, Cl) quantum dots: Potential alternatives for display technology. *ACS Nano* **2015**, *9*, 4533–4542.
- [10] Zhou, Q. C.; Bai, Z. L.; Lu, W. G.; Wang, Y. T.; Zou, B. S.; Zhong, H. Z. *In situ* fabrication of halide perovskite nanocrystal-embedded polymer composite films with enhanced photoluminescence for display backlights. *Adv. Mater.* **2016**, *28*, 9163–9168.
- [11] Wang, Y. N.; He, J.; Chen, H.; Chen, J. S.; Zhu, R. D.; Ma, P.; Towers, A.; Lin, Y.; Gesquiere, A. J.; Wu, S. T. et al. Ultrastable, highly luminescent organic-inorganic perovskite-polymer composite films. *Adv. Mater.* **2016**, *28*, 10710–10717.
- [12] He, J.; Chen, H. W.; Chen, H.; Wang, Y. N.; Wu, S. T.; Dong, Y. J. Hybrid downconverters with green perovskite-polymer composite films for wide color gamut displays. *Opt. Express* **2017**, *25*, 12915–12925.
- [13] Zhang, M. J.; Wang, L. X.; Meng, L. H.; Wu, X. G.; Tan, Q. W.; Chen, Y. J.; Liang, W. Y.; Jiang, F.; Cai, Y.; Zhong, H. Z. Perovskite quantum dots embedded composite films enhancing UV response of silicon photodetectors for broadband and solar-blind light detection. *Adv. Optical Mater.* **2018**, *6*, 1800077.
- [14] Chang, S.; Bai, Z. L.; Zhong, H. Z. *In situ* fabricated perovskite nanocrystals: A revolution in optical materials. *Adv. Optical Mater.* **2018**, *6*, 1800380.
- [15] Wang, D.; Wu, D.; Dong, D.; Chen, W.; Hao, J. J.; Qin, J.; Xu, B.; Wang, K.; Sun, X. W. Polarized emission from CsPbX₃ perovskite quantum dots. *Nanoscale* **2016**, *8*, 11565–11570.
- [16] Liu, L. G.; Huang, S.; Pan, L. F.; Shi, L. J.; Zou, B. S.; Deng, L. G.; Zhong, H. Z. Colloidal synthesis of CH₃NH₃PbBr₃ nanoplatelets with polarized emission through self-organization. *Angew. Chem., Int. Ed.* **2017**, *56*, 1780–1783.
- [17] He, J.; Towers, A.; Wang, Y. N.; Yuan, P. S.; Jiang, Z.; Chen, J. S.; Gesquiere, A. J.; Wu, S. T.; Dong, Y. J. *In situ* synthesis and macroscale alignment of CsPbBr₃ perovskite nanorods in a polymer matrix. *Nanoscale* **2018**, *10*, 15436–15441.
- [18] Raja, S. N.; Bekenstein, Y.; Koc, M. A.; Fischer, S.; Zhang, D. D.; Lin, L. W.; Ritchie, R. O.; Yang, P. D.; Alivisatos, A. P. Encapsulation of perovskite nanocrystals into macroscale polymer matrices: Enhanced stability and polarization. *ACS Appl. Mater. Interfaces* **2016**, *8*, 35523–35533.
- [19] Wang, Z. Y.; Liu, J. Y.; Xu, Z. Q.; Xue, Y. Z.; Jiang, L. C.; Song, J. C.; Huang, F. Z.; Wang, Y. S.; Zhong, Y. L.; Zhang, Y. P. et al. Wavelength-tunable waveguides based on polycrystalline organic-inorganic perovskite microwires. *Nanoscale* **2016**, *8*, 6258–6264.
- [20] Eaton, S. W.; Lai, M. L.; Gibson, N. A.; Wong, A. B.; Dou, L. T.; Ma, J.; Wang, L. W.; Leone, S. R.; Yang, P. D. Lasing in robust cesium lead halide perovskite nanowires. *Proc. Natl. Acad. Sci. USA* **2016**, *113*, 1993–1998.

- [21] Xing, J.; Liu, X. F.; Zhang, Q.; Ha, S. T.; Yuan, Y. W.; Shen, C.; Sum, T. C.; Xiong, Q. H. Vapor phase synthesis of organometal halide perovskite nanowires for tunable room-temperature nanolasers. *Nano Lett.* **2015**, *15*, 4571–4577.
- [22] Gao, L.; Zeng, K.; Guo, J. S.; Ge, C.; Du, J.; Zhao, Y.; Chen, C.; Deng, H.; He, Y. S.; Song, H. S. et al. Passivated single-crystalline $\text{CH}_3\text{NH}_3\text{PbI}_3$ nanowire photodetector with high detectivity and polarization sensitivity. *Nano Lett.* **2016**, *16*, 7446–7454.
- [23] Feng, J. G.; Yan, X. X.; Liu, Y.; Gao, H. F.; Wu, Y. C.; Su, B.; Jiang, L. Crystallographically aligned perovskite structures for high-performance polarization-sensitive photodetectors. *Adv. Mater.* **2017**, *29*, 1605993.
- [24] Sheng, X. X.; Chen, G. Y.; Wang, C.; Wang, W. Q.; Hui, J. F.; Zhang, Q.; Yu, K. H.; Wei, W.; Yi, M. D.; Zhang, M. et al. Polarized optoelectronics of CsPbX_3 ($X = \text{Cl}, \text{Br}, \text{I}$) perovskite nanoplates with tunable size and thickness. *Adv. Funct. Mater.* **2018**, *28*, 1800283.
- [25] Oener, S. Z.; Khoram, P.; Brittan, S.; Mann, S. A.; Zhang, Q. P.; Fan, Z. Y.; Boettcher, S. W.; Garnett, E. C. Perovskite nanowire extrusion. *Nano Lett.* **2017**, *17*, 6557–6563.
- [26] Gu, L. L.; Tavakoli, M. M.; Zhang, D. Q.; Zhang, Q. P.; Waleed, A.; Xiao, Y. Q.; Tsui, K. H.; Lin, Y. J.; Liao, L.; Wang, J. N. et al. 3D Arrays of 1,024-pixel image sensors based on lead halide perovskite nanowires. *Adv. Mater.* **2016**, *28*, 9713–9721.
- [27] Liu, P.; He, X. X.; Ren, J. H.; Liao, Q.; Yao, J. N.; Fu, H. B. Organic-inorganic hybrid perovskite nanowire laser arrays. *ACS Nano* **2017**, *11*, 5766–5773.
- [28] Deng, W.; Huang, L. M.; Xu, X. Z.; Zhang, X. J.; Jin, X. C.; Lee, S. T.; Jie, J. S. Ultrahigh-responsivity photodetectors from perovskite nanowire arrays for sequentially tunable spectral measurement. *Nano Lett.* **2017**, *17*, 2482–2489.
- [29] Lu, W. G.; Wu, X. G.; Huang, S.; Wang, L.; Zhou, Q. C.; Zou, B. S.; Zhong, H. Z.; Wang, Y. T. Strong polarized photoluminescence from stretched perovskite nanocrystal embedded polymer composite films. *Adv. Optical Mater.* **2017**, *5*, 1700594.
- [30] Güner, T.; Topçu, G.; Savacı, U.; Genç, A.; Turan, S.; Sari, E.; Demir, M. M. Polarized emission from CsPbBr_3 nanowire embedded-electrospun PU fibers. *Nanotechnology* **2018**, *29*, 135202.
- [31] Bhardwaj, N.; Kundu, S. C. Electrospinning: A fascinating fiber fabrication technique. *Biotechnol. Adv.* **2010**, *28*, 325–347.
- [32] Wang, Y. W.; Zhu, Y. H.; Huang, J. F.; Cai, J.; Zhu, J. R.; Yang, X. L.; Shen, J. H.; Jiang, H.; Li, C. Z. CsPbBr_3 perovskite quantum dots-based monolithic electrospun fiber membrane as an ultrastable and ultrasensitive fluorescent sensor in aqueous medium. *J. Phys. Chem. Lett.* **2016**, *7*, 4253–4258.
- [33] Yang, M. S.; Yu, J.; Jiang, S. Z.; Zhang, C.; Sun, Q. Q.; Wang, M. H.; Zhou, H.; Li, C. H.; Man, B. Y.; Lei, F. C. High stability luminophores: Fluorescent CsPbX_3 ($X = \text{Cl}, \text{Br}$ and I) nanofiber prepared by one-step electrospinning method. *Opt. Express* **2018**, *26*, 20649–20660.
- [34] Liao, H.; Guo, S. B.; Cao, S.; Wang, L.; Gao, F. M.; Yang, Z. B.; Zheng, J. J.; Yang, W. Y. A general strategy for *in situ* growth of all-inorganic CsPbX_3 ($X = \text{Br}, \text{I}$, and Cl) perovskite nanocrystals in polymer fibers toward significantly enhanced water/thermal stabilities. *Adv. Optical Mater.* **2018**, *6*, 1800346.
- [35] Lin, C. C.; Jiang, D. H.; Kuo, C. C.; Cho, C. J.; Tsai, Y. H.; Satoh, T.; Su, C. Water-resistant efficient stretchable perovskite-embedded fiber membranes for light-emitting diodes. *ACS Appl. Mater. Interfaces* **2018**, *10*, 2210–2215.
- [36] Tsai, P. C.; Chen, J. Y.; Ercan, E.; Chueh, C. C.; Tung, S. H.; Chen, W. C. Uniform luminous perovskite nanofibers with color-tunability and improved stability prepared by one-step core/shell electrospinning. *Small* **2018**, *14*, 1704379.
- [37] Han, M. H.; Shin, J. K.; Oh, K. I.; Lee, Y. J.; Song, D. H.; Chung, Y. S.; Lee, Y. R.; Choi, H. G.; Oh, T. H.; Han, S. S. et al. Preparation of recycled poly(vinyl alcohol) (PVA)/iodine polarizing film. *Polym. Polym. Compos.* **2010**, *18*, 391–396.
- [38] Zhang, F.; Chen, C.; Kershaw, S. V.; Xiao, C. T.; Han, J. B.; Zou, B. S.; Wu, X.; Chang, S.; Dong, Y. P.; Rogach, A. L. et al. Ligand-controlled formation and photoluminescence properties of $\text{CH}_3\text{NH}_3\text{PbBr}_3$ nanocubes and nanowires. *ChemNanoMat* **2017**, *3*, 303–310.
- [39] Rodina, A. V.; Efros, A. L. Effect of dielectric confinement on optical properties of colloidal nanostructures. *J. Exp. Theor. Phys.* **2016**, *122*, 554–566.
- [40] Ruda, H. E.; Shik, A. Polarization-sensitive optical phenomena in semiconducting and metallic nanowires. *Phys. Rev. B* **2005**, *72*, 115308.
- [41] Schneider, J.; Zhang, W. L.; Srivastava, A. K.; Chigrinov, V. G.; Kwok, H. S.; Rogach, A. L. Photoinduced micropattern alignment of semiconductor nanorods with polarized emission in a liquid crystal polymer matrix. *Nano Lett.* **2017**, *17*, 3133–3138.
- [42] Shabaev, A.; Efros, A. L. 1D exciton spectroscopy of semiconductor nanorods. *Nano Lett.* **2004**, *4*, 1821–1825.
- [43] Chamarro, M.; Gourdon, C.; Lavallard, P. Photoluminescence polarization of semiconductor nanocrystals. *J. Lumin.* **1996**, *70*, 222–237.
- [44] Zhang, G. F.; Peng, Y. G.; Xie, H. Q.; Li, B.; Li, Z. J.; Yang, C. G.; Guo, W. L.; Qin, C. B.; Chen, R. Y.; Gao, Y. et al. Linear dipole behavior of single quantum dots encased in metal oxide semiconductor nanoparticles films. *Front. Phys.* **2018**, *14*, 23605.
- [45] Hu, J. T.; Li, L. S.; Yang, W. D.; Manna, L.; Wang, L. W.; Alivisatos, A. P. Linearly polarized emission from colloidal semiconductor quantum rods. *Science* **2001**, *292*, 2060–2063.
- [46] Peng, X. G.; Manna, L.; Yang, W. D.; Wickham, J.; Scher, E.; Kadavanich, A.; Alivisatos, A. P. Shape control of CdSe nanocrystals. *Nature* **2000**, *404*, 59–61.
- [47] Diroll, B. T.; Dadosh, T.; Koschitzky, A.; Goldman, Y. E.; Murray, C. B. Interpreting the energy-dependent anisotropy of colloidal nanorods using ensemble and single-particle spectroscopy. *J. Phys. Chem. C* **2013**, *117*, 23928–23937.
- [48] Tice, D. B.; Weinberg, D. J.; Mathew, N.; Chang, R. P. H.; Weiss, E. A. Measurement of wavelength-dependent polarization character in the absorption anisotropies of ensembles of CdSe nanorods. *J. Phys. Chem. C* **2013**, *117*, 13289–13296.
- [49] Giblin, J.; Protasenko, V.; Kuno, M. Wavelength sensitivity of single nanowire excitation polarization anisotropies explained through a generalized treatment of their linear absorption. *ACS Nano* **2009**, *3*, 1979–1987.
- [50] Sitt, A.; Salant, A.; Menagen, G.; Banin, U. Highly emissive nano rod-in-rod heterostructures with strong linear polarization. *Nano Lett.* **2011**, *11*, 2054–2060.
- [51] Tauber, D.; Dobrovolsky, A.; Camacho, R.; Scheblykin, I. G. Exploring the electronic band structure of organometal halide perovskite via photoluminescence anisotropy of individual nanocrystals. *Nano Lett.* **2016**, *16*, 5087–5094.
- [52] Wang, J. F.; Gudiksen, M. S.; Duan, X. F.; Cui, Y.; Lieber, C. M. Highly polarized photoluminescence and photodetection from single indium phosphide nanowires. *Science* **2001**, *293*, 1455–1457.
- [53] Cunningham, P. D.; Boercker, J. E.; Placencia, D.; Tischler, J. G. Anisotropic absorption in PbSe nanorods. *ACS Nano* **2014**, *8*, 581–590.
- [54] Diroll, B. T.; Koschitzky, A.; Murray, C. B. Tunable optical anisotropy of seeded CdSe/CdS nanorods. *J. Phys. Chem. Lett.* **2014**, *5*, 85–91.
- [55] Lavallard, P.; Suris, R. A. Polarized photoluminescence of an assembly of non cubic microcrystals in a dielectric matrix. *Solid State Commun.* **1995**, *95*, 267–269.
- [56] Tanaka, K.; Takahashi, T.; Ban, T.; Kondo, T.; Uchida, K.; Miura, N. Comparative study on the excitons in lead-halide-based perovskite-type crystals $\text{CH}_3\text{NH}_3\text{PbBr}_3$ $\text{CH}_3\text{NH}_3\text{PbI}_3$. *Solid State Commun.* **2003**, *127*, 619–623.
- [57] Hasegawa, M.; Hirayama, Y. Use of quantum rods for display applications. *SID Symp. Dig. Tech. Pap.* **2016**, *47*, 241–244.
- [58] Qin, J.; Wen, Z. L.; Li, S.; Hao, J. J.; Chen, W.; Dong, D.; Deng, J.; Wang, D.; Xu, B.; Wu, D. et al. Large-scale luminance enhancement film with quantum rods aligned in polymeric nanofibers for high efficiency wide color gamut LED display. *SID Symp. Dig. Tech. Pap.* **2016**, *47*, 854–857.